ARMY RESEARCH LABORATORY

Multiscale Modeling of Deformation Twinning Based on Field Theory of Multiscale Plasticity (FTMP)

by Tadashi Hasebe and John D. Clayton

ARL-TR-6581 **September 2013**

NOTICES

Disclaimers

The findings in this report are not to be construed as an official Department of the Army position unless so designated by other authorized documents.

Citation of manufacturer's or trade names does not constitute an official endorsement or approval of the use thereof.

Destroy this report when it is no longer needed. Do not return it to the originator.

Army Research Laboratory
Aberdeen Proving Ground, MD 21005-5069

ARL-TR-6581 **September 2013**

Multiscale Modeling of Deformation Twinning Based on Field Theory of Multiscale Plasticity (FTMP)

Tadashi Hasebe
Kobe University

John D. Clayton
Weapons and Materials Research Directorate, ARL

REPORT DOCUMENTATION PAGE	Form Approved OMB No. 0704-0188

1. REPORT DATE *(DD-MM-YYYY)*	2. REPORT TYPE	3. DATES COVERED (From - To)
September 2013	Final	October 2012–June 2013

4. TITLE AND SUBTITLE
Multiscale Modeling of Deformation Twinning Based on Field Theory of Multiscale Plasticity (FTMP)

5a. CONTRACT NUMBER

5b. GRANT NUMBER

5c. PROGRAM ELEMENT NUMBER

6. AUTHOR(S)
Tadashi Hasebe* and John D. Clayton

5d. PROJECT NUMBER

5e. TASK NUMBER

5f. WORK UNIT NUMBER

7. PERFORMING ORGANIZATION NAME(S) AND ADDRESS(ES)
U.S. Army Research Laboratory
ATTN: RDRL-WMP-C
Aberdeen Proving Ground, MD 21005-5066

8. PERFORMING ORGANIZATION REPORT NUMBER
ARL-TR-6581

9. SPONSORING/MONITORING AGENCY NAME(S) AND ADDRESS(ES)

10. SPONSOR/MONITOR'S ACRONYM(S)

11. SPONSOR/MONITOR'S REPORT NUMBER(S)

12. DISTRIBUTION/AVAILABILITY STATEMENT
Approved for public release; distribution is unlimited.

13. SUPPLEMENTARY NOTES
*Department of Mechanical Engineering, Kobe University, 1-1 Rokkodai, Nada, Kobe 657-8501, Japan

14. ABSTRACT
In this report, we discuss the application of a field theory, incorporating first and second gradients of plastic distortion into the constitutive response of metallic single crystals. Differential-geometric aspects of the theory are briefly summarized, and a constitutive model for ductile crystals is then outlined. We also report simulations that confirm basic capabilities of the model in terms of describing important features of deformation twinning, e.g., nucleation, growth, lattice rotation, and the attendant stress response and energy redistribution. Using numerical results for face-centered cubic metals—single crystals and polycrystalline samples of copper—we examine the effects of geometrical constraints. Numerical results for hexagonal close-packed metals—specifically, magnesium single crystals—demonstrate interactions between twinning and slip, tension-compression asymmetry, reversibility, and other typically observed properties. Agreement with experiments is satisfactory.

15. SUBJECT TERMS
multiscale modeling, plasticity, twinning, metals

16. SECURITY CLASSIFICATION OF:			17. LIMITATION OF ABSTRACT	18. NUMBER OF PAGES	19a. NAME OF RESPONSIBLE PERSON
a. REPORT	b. ABSTRACT	c. THIS PAGE			John D. Clayton
Unclassified	Unclassified	Unclassified	UU	30	19b. TELEPHONE NUMBER (*Include area code*) 410-278-6146

Contents

List of Figures

Acknowledgments

Support of the work of the principal investigator (T. Hasebe) through contract no. FA5209-13-P-0043 jointly by U.S. Army Research, Development, and Engineering Command International Technology Center Pacific (K. Park) and the Materials and Manufacturing Sciences Division of the U.S. Army Research Laboratory's Weapons and Materials Research Directorate (H. Maupin and J. Zabinski) is gratefully acknowledged.

INTENTIONALLY LEFT BLANK.

1. Introduction

A physical restriction in most conventional continuum models is their inability of taking into account sufficient microscopic degrees of freedom in the constitutive framework. For crystalline metallic materials, the dislocation-related microstructural degrees of freedom responsible for dislocation substructure evolution are critically important to model and simulate multiscale aspects of plastically deforming metals. A solution to this problem has been recently provided by the Field Theory of Multiscale Plasticity (FTMP) advocated by Hasebe (*1–4*). In this relatively new theoretical framework, additional degrees of freedom are implemented via FTMP-based tensor of incompatibility derived from the differential geometric curvature tensor constructed from gradients of the metric tensor of the plastically deformed (or elastically unloaded) incompatible/anholonomic crystalline space (*4–6*), to be ultimately incorporated in a crystalline plasticity-based constitutive framework.

In this work, we propose a new model for deformation twinning based on FTMP. Twinning is an alternative mode of plastic deformation to slip via dislocation glide, the former involving collective motion of partial dislocations. Deformation twinning is a major deformation mode for hexagonal close-packed (HCP) metals (here HCP refers to any hexagonal metal, not necessarily one with the ideal c/a ratio for closest packing, where c and a are lattice parameters of the hexagonal unit cell) and also for some face-centered cubic (FCC) metals with low stacking fault energy (SFE) (e.g., less than 25 mJ/m^2) and in body-centered cubic (BCC) metals under high strain rates and/or low temperatures. Even in FCC metals with intermediate SFE around 50–70 mJ/m^2, such as copper (Cu) and nickel (Ni), where most plastic deformation can be carried by glide of dislocations, mechanical twinning can still take place, e.g., under hypervelocity impact loading. Since both twinning and slip resistance can be affected by densities of continuously distributed dislocations introduced via accommodation of excessive local deformation, extended use of the incompatibility tensor-based model is expected be effective for their descriptions.

In this report, a brief theoretical overview and a "flow-evolutionary working hypothesis" are given in section 2. The constitutive framework is outlined in sections 3 (slip) and 4 (twinning). Representative results from deformation simulations of cubic and hexagonal metallic crystals (Cu and magnesium [Mg], respectively) are presented in sections 5 and 6. Bold font is used for vectors and tensors and italic for scalars with summation over repeated indices.

2. Theoretical Background

2.1 Differential Geometric Description of Defect Fields

Let ∇ denote the covariant derivative with respect to arbitrary connection $\boldsymbol{\Gamma}$. In spatial coordinates x^i (i = 1,2,3), the covariant derivative of a smooth vector field $\boldsymbol{V}(\boldsymbol{x})$ is

$$\nabla_i V^j = \partial_i V^j + \Gamma^j_{ik} V^k . \tag{1}$$

The covariant derivative of the space itself can be defined by

$$(\nabla \boldsymbol{x})^i \equiv (\partial_k x^i + \Gamma^i_{kl} x^l) dx^k = dx^i + \Gamma^i_{kl} x^l \, dx^k . \tag{2}$$

Let indices in brackets be skew, indices in parentheses be symmetric, and indices in vertical bars be excluded from such operations, e.g.,

$$2A_{[ij]} = A_{ij} - A_{ji}, \quad 2A_{(ij)} = A_{ij} + A_{ji}, \quad 2B_{[i|j|k]} = B_{ijk} - B_{kji} . \tag{3}$$

Torsion and curvature tensors are defined, respectively, for a generic connection as

$$S^{\cdot\cdot j}_{kl} = \Gamma^j_{[kl]}, \qquad R^{\cdots n}_{klm} = 2(\partial_{[k}\Gamma^n_{l]m} + \Gamma^n_{[k|p|}\Gamma^p_{l]m}) . \tag{4}$$

When torsion $\boldsymbol{S}$ is nonzero, coefficients of $\boldsymbol{\Gamma}$ describe a non-Riemannian space. When curvature $\boldsymbol{R}$ vanishes, the space is said to be flat.

In finite deformation plasticity, a multiplicative decomposition of the deformation gradient $\boldsymbol{F}$ into elastic and plastic terms is standard:

$$\boldsymbol{F} = \partial \boldsymbol{x} / \partial \boldsymbol{X} = \boldsymbol{F}^e \cdot \boldsymbol{F}^p \simeq \mathbf{1} + \boldsymbol{\beta}^e + \boldsymbol{\beta}^p , \tag{5}$$

where in the final approximation, small deformations are assumed such that, for the displacement field $\boldsymbol{u}$, in Cartesian coordinates, elastic and plastic distortions are additive:

$$\partial u_j / \partial X_i \simeq \partial u_j / \partial x_i = \partial_i u_j = \beta^e_{ji} + \beta^p_{ji} . \tag{6}$$

Two connections are introduced:

$$\bar{\Gamma}^i_{jk} \equiv F^{ei}_{\cdot\alpha} \partial_j F^{e-1\alpha}_{\cdot k}, \qquad \tilde{\Gamma}^i_{jk} \equiv \tfrac{1}{2} C^{e-1il} (\partial_j C^e_{lk} + \partial_k C^e_{lj} - \partial_l C^e_{jk}) \qquad \left[\boldsymbol{C}^e \equiv \boldsymbol{F}^{e-\mathrm{T}} \cdot \boldsymbol{F}^{e-1} \right]. \tag{7}$$

The first has vanishing curvature but nonvanishing torsion $\bar{\boldsymbol{S}}$, and the second has vanishing torsion but nonvanishing curvature $\tilde{\boldsymbol{R}}$. Contractions of these higher-order tensors considering symmetry results in well-known second-order tensors. They are respectively called “dislocation density tensor” and “incompatibility tensor,” given in the geometrically linear regime by the curl of the elastic or plastic distortion tensor and double curl of the elastic or plastic strain tensor:

$$\alpha^{ij} = -\varepsilon^{ikl}\bar{S}^{\cdot\cdot j}_{kl} \simeq \varepsilon^{ikl}\partial_k \beta^{e\,j}_{\cdot l} = -\varepsilon^{ikl}\partial_k \beta^{p\,j}_{\cdot l}, \tag{8}$$

$$\eta^{ij} = \tfrac{1}{4}\varepsilon^{ikl}\varepsilon^{jmn}\tilde{R}_{klmn} \simeq -\varepsilon^{ikl}\varepsilon^{jmn}\partial_k\partial_m\varepsilon^e_{ln} = \varepsilon^{ikl}\varepsilon^{jmn}\partial_k\partial_m\varepsilon^p_{ln}, \tag{9}$$

where elastic and plastic strains are $\varepsilon^e_{ln} = \beta^e_{(ln)}$ and $\varepsilon^p_{ln} = \beta^p_{(ln)}$, and where $\varepsilon^{ikl} = g^{-1/2}e^{ikl}$ with $g = \det[g_{ij}] = \det[\partial_i \boldsymbol{x}\cdot\partial_j \boldsymbol{x}]$ and e^{ikl} is the dimensionless alternator symbol. In the right two equalities of equation 9, terms on the order of the square of the connection coefficients are assumed small relative to strain gradients. Complete derivations can be found elsewhere (*4*, *6*, *7*). Henceforth, Cartesian coordinates are used ($g_{ij} = \delta_{ij}$), and linearized tensors in equations 8 and 9 are

$$\alpha_{ij} = \varepsilon_{ikl}\partial_l \beta^p_{kj}, \qquad \eta_{ij} = e_{ikl}e_{jmn}\partial_k\partial_m\varepsilon^p_{ln}. \tag{10}$$

The important point to note here is that these quantities are expressed as gradients of plastic distortion or plastic strain, meaning the theory intrinsically requires strain gradients at least up to the second order.

2.2 Flow-Evolutionary Hypothesis in FTMP

Hasebe's "flow-evolutionary hypothesis" asserts laws for evolution of inhomogeneous fields and attendant local plastic flow accompanied by energy dissipation. The notion of "duality" between fluctuating hydrostatic stress and deviatoric strain fields introduced in FTMP (*2–4*) can be embodied by this law, although it still is a "working hypothesis" deserving further verification and validation. Specifically, it represents an interrelationship between locally stored strain energy (fluctuation part) and local plastic flow (in the form of incompatibility tensor field $\boldsymbol{\eta}$) as has been discussed in the context of polycrystalline plasticity (*8*). A brief motivation for this hypothesis follows.

Consider an elastic medium with internal energy density $\mathcal{W}$ and kinetic energy density $\mathcal{K}$:

$$\mathcal{W} = \mathcal{W}(\boldsymbol{\varepsilon}, \boldsymbol{x}), \quad \mathcal{K} = \tfrac{1}{2}\rho\boldsymbol{v}\cdot\boldsymbol{v}, \quad \mathcal{L} = \mathcal{K} - \mathcal{W}, \quad \mathcal{H} = \mathcal{K} + \mathcal{W}. \tag{11}$$

Here, $\mathcal{L}$ and $\mathcal{H}$ are the Lagrangian and Hamiltonian energy densities, respectively. Let the Cauchy stress be $\boldsymbol{\sigma} = \partial\mathcal{W}/\partial\boldsymbol{\varepsilon}$ and the energy momentum tensor be (*9*)

$$T_{ij} = -(\mathcal{L}\delta_{ij} + \sigma_{ik}\partial_j u_k), \qquad \partial_j T_{ij} + \rho\partial(v_j\partial_j u_i)/\partial t = -f_i = (\partial\mathcal{L}/\partial x_i)|_{\exp}. \tag{12}$$

Here, $\boldsymbol{f}$ is the local force per unit volume acting on an inhomogeneity or defect.

In the static case, and when $\mathcal{W} = \mathcal{W}(\boldsymbol{\varepsilon})$, i.e., the body contains no heterogeneities, then $\boldsymbol{T}$ is divergence-free. The incompatibility tensor is symmetric and divergence-free:

$$\partial_j\eta_{ij} = \partial_j\eta_{ji} = e_{jkl}e_{imn}\partial_j\partial_k\partial_m\varepsilon^p_{ln} = e_{[jk]l}e_{imn}\partial_{(j}\partial_{k)}\partial_m\varepsilon^p_{ln} = 0. \tag{13}$$

Under these assumptions, since both energy-momentum tensor and incompatibility tensor are divergence-free, the following linear relationship can be postulated:

$$\eta_{ij} = \kappa_{ijkl}\delta T_{kl}, \qquad \kappa_{ijkl} = \tfrac{1}{2}\kappa(\delta_{ik}\delta_{jl} + \delta_{il}\delta_{jk}), \tag{14}$$

where isotropy is assumed in the definition of the constants κ_{ijkl}, so that the first of equation 14 is

$$\eta_{ij} = \kappa\delta T_{(ij)} \Rightarrow \partial_j \eta_{ij} = \kappa\partial_j \delta T_{(ij)} = 0, \tag{15}$$

consistent with the vanishing divergence requirement if the skew part of $\boldsymbol{T}$ is divergence-free and/or vanishing. Equation 15 can be inverted to give

$$\delta T_{(ij)} = \mu l^2 \eta_{ij}, \tag{16}$$

where μ is the shear modulus and l a length constant. Physically, equation 14 appears sensible since the energy-momentum tensor is a driving force for the evolution or motion of defects, which, in turn, are represented by incompatibility. A complementary hypothesis is (*4*)

$$\mathrm{tr}\boldsymbol{\eta} \propto \delta\mathcal{H} = \delta\left(\mathcal{K} + \mathcal{W}\right), \tag{17}$$

which can be formulated using the 4-D permutation tensor entering the generalized cross product (*10*). The proposed relationship between incompatibility and elastic energy will be further explored in the context of numerical results in section 5.2.

3. Constitutive Framework

3.1 Shear Stress–Shear Strain Relationship

As a tentative vehicle for accommodating the field theoretical concepts overviewed in the previous section to practical applications, the kinematical foundations of crystal plasticity are utilized. The constitutive equation to be used, on the other hand, puts its basis on the statistical mechanics-based dislocation dynamics with which wide ranges of strain rate and temperature can be taken into account in a unified manner.

The current field theoretical notions and quantities, including the interaction field framework, can be easily implemented into the crystalline plasticity model through strain gradient terms (*8*, *11*, *12*). Hasebe proposed a constitutive model applicable to FCC, BCC, and HCP metals based on statistical mechanics and dislocation dynamics. The rate of plastic distortion is the usual form from crystal plasticity theory:

$$\dot{\boldsymbol{F}}^p \simeq \dot{\boldsymbol{\beta}}^p = \sum_{\alpha=1}^{N} \dot{\gamma}^\alpha \boldsymbol{s}^\alpha \otimes \boldsymbol{m}^\alpha, \tag{18}$$

with $\boldsymbol{s}^\alpha$ and $\boldsymbol{m}^\alpha$ the slip direction and plane normal for system α. The explicit form for slip rates due to resolved shear stress $\tau^\alpha = \boldsymbol{\sigma} : \boldsymbol{s}^\alpha \otimes \boldsymbol{m}^\alpha$ is (*8*, *11*)

$$\dot{\gamma}^\alpha = A_S \tau'^\alpha \left\{ |\tau'^\alpha| B_S \exp\left[1-(\tau'^\alpha / K^\alpha)^p\right]^q + C_S \right\}^{-1}, \qquad \tau'^\alpha \equiv \left\langle \tau^\alpha - \tau_P^\alpha \right\rangle - \Omega^\alpha . \tag{19}$$

Here, $A_S = \rho_m b L \upsilon$, $B_S = \Delta G_0 / k_B T$, $C_S = BL\upsilon / b$, where K^α and Ω^α are drag and back stress, respectively, responsible for isotropic and kinematic hardening; ρ_m, L, υ, b, and B are mobile dislocation density, mean flying distance of dislocations, modified Debye frequency, the magnitude of Burgers vector and the damping coefficient due to, e.g., phonon drag, respectively; and ΔG_0 is activation energy for dislocation processes at T = 0 K. Exponents p and q in equation 19 are parameters specifying thermal obstacles of interest, provided $0 \le p \le 1$ and $1 \le q \le 2$. In the standard case, $p = \frac{1}{2}$, $q = \frac{3}{2}$ is used for representing dislocation processes. Furthermore, $\langle \bullet \rangle \equiv \frac{1}{2}(|\bullet| + \bullet)$ is the Macaulay parentheses, with $\tau_p^{(\alpha)}$ expressing the effective stress for overcoming the Peierls process given by

$$\tau_p^\alpha = \left[1 - \left(\frac{k_B T}{g_0^P \mu b^3} \ln \frac{\dot{\gamma}_0}{\dot{\gamma}^{\alpha)}} \right)^{1/q_P} \right]^{1/p_P}, \tag{20}$$

where g_0^P, $\dot{\gamma}_0$, p_P, and q_P are parameters for thermal activation via the Peierls overcoming event. This constitutive model can express stress-strain responses for FCC, HCP, and BCC metals over a wide range of strain rates and temperatures, including impact loading conditions. For BCC, typically $C_S \simeq 0$; for FCC and HCP, typically $\tau_P^\alpha / K^\alpha \simeq 0$.

3.2 Drag Stress Model

The hardening evolution models are affected through drag stress K^α. The interactions of dislocation against forests (or equivalently, interactions among dislocations mostly belong to different slip systems) are regarded as being primarily responsible for the additional hardening. The quality of the additional hardening, i.e., "history," is characterized by the effective cell size to be defined as follows via hardening ratio.

The time evolution of the drag stress defines the instantaneous hardening modulus and is assumed to be expressed as the following form:

$$\dot{K}^\alpha = \sum_{\alpha=1}^N Q_{\alpha\beta} H(\gamma) |\dot{\gamma}^\beta| = \sum_{\alpha=1}^N \frac{\partial \tau^\alpha}{\partial \tau_{ref}} \cdot \frac{\partial \tau_{ref}}{\partial \gamma^\beta} |\dot{\gamma}^\beta|, \tag{21}$$

where $H(\gamma) \equiv \partial \tau_{ref} / \partial \gamma$ is the referential hardening modulus with no interaction among slip systems, while $Q_{\alpha\beta}$ denotes the hardening ratio that evolves with histories and interactions. In order to express the nonlocal actions associated with the evolution of inhomogeneities based on dislocation density and incompatibility fields, strain gradient terms are additively introduced into $Q_{\alpha\beta}$ as discussed in section 3.3.

Dimensionless hardening ratio $Q_{\alpha\beta}$ expresses the ratio of the flow stress increase to the referential level, measuring the additional hardening, and is further used to evaluate the effective cell size, because it, in principle, contains all the information about the dislocation cells evolved (responsible for the additional hardening). Therefore, we can assume that the quantity characterizes an effective size of dislocation cells, defined here as (*12*)

$$d = d_0 \left[\left(\sum\nolimits_{\alpha,\beta} Q_{\alpha\beta} Q_{\alpha\beta} \right) \Big/ N \right]^{-1/2}, \tag{22}$$

where d_0 represents the initial cell size, normally a fraction of the initial grain size.

3.3 Hardening Law and Field Theoretical Strain Gradient Terms

The model incorporates contributions of $\boldsymbol{\alpha}$ and $\boldsymbol{\eta}$ through hardening ratio $Q_{\alpha\beta}$ as (*11*)

$$Q_{\alpha\beta} = \sum\nolimits_{\kappa=1}^{N} f_{\alpha\kappa} S_{\kappa\beta} + \delta_{\alpha\beta} \left[1 + F^{\alpha}(\boldsymbol{\alpha}, \boldsymbol{\eta}) \right], \tag{23}$$

where $f_{\alpha\kappa}$ represents the dislocation interaction matrix and $S_{\kappa\beta}$ expresses a history matrix further given as an increasing function of plastic work done by the effective stress that is responsible for dislocation processes:

$$S_{\alpha\beta} = \tanh\left(W_{\alpha\beta}^{P} \big/ W_{sat} \right), \qquad W_{\alpha\beta}^{P} = \delta_{\alpha\beta} W_{P}^{\beta} \quad \text{(no sum)}. \tag{24}$$

Here, W_P^{β} defines the plastic work done by the effective stress for only the dislocation processes:

$$W_P^{\beta} = \int \dot{W}_P^{\beta} \mathrm{d}t = \int \left\langle \tau^{\beta} - \tau_P^{\beta} \right\rangle \dot{\gamma}^{\beta} \mathrm{d}t \,. \tag{25}$$

Function $F^{\beta}(\alpha^{\beta}; \eta^{\beta}) \equiv F_1^{\beta}(\alpha^{\beta}) + F_2^{\beta}(\eta^{\beta})$ expresses the field theoretical "strain gradient term" contributions (*8*):

$$F_1^{\beta}(\alpha^{\beta}) = \left(k / p_{\beta} \right) \left(|\alpha^{\beta}| / b \right)^{1/2}, \qquad F_2^{\beta}(\eta^{\beta}) = \left(k / q_{\beta} \right) \left(l_d \, |\eta^{\beta}| / b \right)^{1/2} \mathrm{sgn}(\eta^{\beta}), \tag{26}$$

where p_{β}, q_{β} are coefficients related to contributions of dislocations and incompatibility to the change in the effective cell size d, while l_d represents the characteristic length of the defect field considered, e.g., $l_d = b$ for dislocation dipoles and $l_d \approx 10^{-6}\,\mathrm{m}$ for substructures like cells. Here, α^{β} and η^{β} are resolved components of α_{ij} and η_{ij}, respectively:

$$\alpha^{\beta} = [(\boldsymbol{s}^{\beta} \times \boldsymbol{m}^{\beta}) \otimes \boldsymbol{s}^{\beta} + \boldsymbol{s}^{\beta} \otimes \boldsymbol{s}^{\beta}] : \boldsymbol{\alpha}, \quad \eta^{\beta} = [(\boldsymbol{s}^{\beta} \times \boldsymbol{m}^{\beta}) \otimes \boldsymbol{s}^{\beta} + \boldsymbol{s}^{\beta} \otimes \boldsymbol{s}^{\beta} + \boldsymbol{s}^{\beta} \otimes \boldsymbol{m}^{\beta}] : \boldsymbol{\eta}. \tag{27}$$

The first and second terms in brackets respectively correspond to edge and screw components of dislocation density. A similar assertion can be made for incompatibility, where the third will be called disclination type, though not corresponding to disclination theory in (*6*).

4. Modeling Deformation Twinning

The elastic-plastic decomposition (equation 5) is extended to allow for twinning deformation (*13*):

$$\boldsymbol{F}=\boldsymbol{F}^{e}\cdot\boldsymbol{F}^{t}\cdot\boldsymbol{F}^{p}\simeq\mathbf{1}+\boldsymbol{\beta}^{e}+\boldsymbol{\beta}^{t}+\boldsymbol{\beta}^{p}. \tag{28}$$

Deformation for twinning is represented by $\boldsymbol{F}^{t}$ with approximate time rate

$$\dot{\boldsymbol{F}}^{t}\simeq\dot{\boldsymbol{\beta}}^{t}=\sum\nolimits_{\chi=1}^{M}\dot{\gamma}^{\chi}\boldsymbol{s}^{\chi}\otimes\boldsymbol{m}^{\chi}, \tag{29}$$

with twinning direction $\boldsymbol{s}^{\chi}$, habit plane normal $\boldsymbol{m}^{\chi}$, and shearing rate $\dot{\gamma}^{\chi}$, which can be expressed in terms of the change in mass fraction of the twinned volume and the quantized maximum twinning shear (*6, 13*). The geometrically nonlinear version of the model implements the Jaumann rate of the Kirchhoff stress tensor $\tau=(\det\boldsymbol{F})\boldsymbol{\sigma}$. In the geometrically linear regime, Cauchy stress is given by

$$\sigma_{ij}=C_{ijkl}\beta^{e}_{kl}=C_{ijkl}(\partial_{l}u_{k}-\beta^{t}_{kl}-\beta^{p}_{kl}),\qquad C_{ijkl}=\partial^{2}\mathcal{W}\big/\partial\varepsilon^{e}_{ij}\partial\varepsilon^{e}_{kl}. \tag{30}$$

The strain rate due to deformation twinning is assumed to be driven by the evolution of the incompatibility tensor field for the twinning mode, $\eta^{\chi}\equiv[(\boldsymbol{s}^{\chi}\times\boldsymbol{m}^{\chi})\otimes\boldsymbol{s}^{\chi}]:\boldsymbol{\eta}$, i.e.,

$$\dot{\gamma}^{\chi}=\sum\nolimits_{\beta}Q^{t}_{\chi\beta}\left|\dot{\gamma}^{\beta}_{prev}\right|,\qquad Q^{t}_{\chi\beta}=\delta_{\chi\beta}F_{3}\left\langle 1-F_{3}\big/F_{3}^{sat}\right\rangle. \tag{31}$$

Here, $F_{3}(\eta^{\chi})$ denotes the FTMP-based incompatibility term defined as

$$F_{3}\equiv\left(k/q_{\chi}\right)\left(\eta^{\chi}l_{t}/b\right)^{1/2}\operatorname{sgn}(\eta^{\chi}). \tag{32}$$

5. Numerical Simulations: FCC Copper (Cu)

5.1 Model, Results, and Discussion

The FTMP-based incompatibility model corresponding to slip and twinning degrees of freedom has been introduced into the hardening law in a crystalline plasticity-based constitutive equation applied to FCC Cu. The model has been implemented by Hasebe in an original finite-element method (FEM) code for static implicit analysis. Tension/compression analyses are conducted on a single slip–oriented single crystal to check basic capabilities of the model for describing several typical features of the deformation twinning: nucleation, growth (into, e.g., lenticular shapes), lattice rotation (satisfying the mirror symmetry), the attendant stress responses to be accompanied by softening with serrations, and energy redistribution into the twin degrees of

freedom. Similar analyses are carried out on multigrain samples (composed of seven grains) and larger polycrystalline samples to systematically investigate the effects of geometrically induced inhomogeneity on nucleation and growth of multiple twins and the attendant stress-strain responses.

Figure 1 shows the domain analyzed in the present series of finite-element (FE) simulations, with 24 × 24 cross triangle elements for plane stress conditions. The sample is pulled in a single slip orientation $[12\bar{5}]$ to up to $\varepsilon = 0.20$ (i.e., 20% tensile elongation).

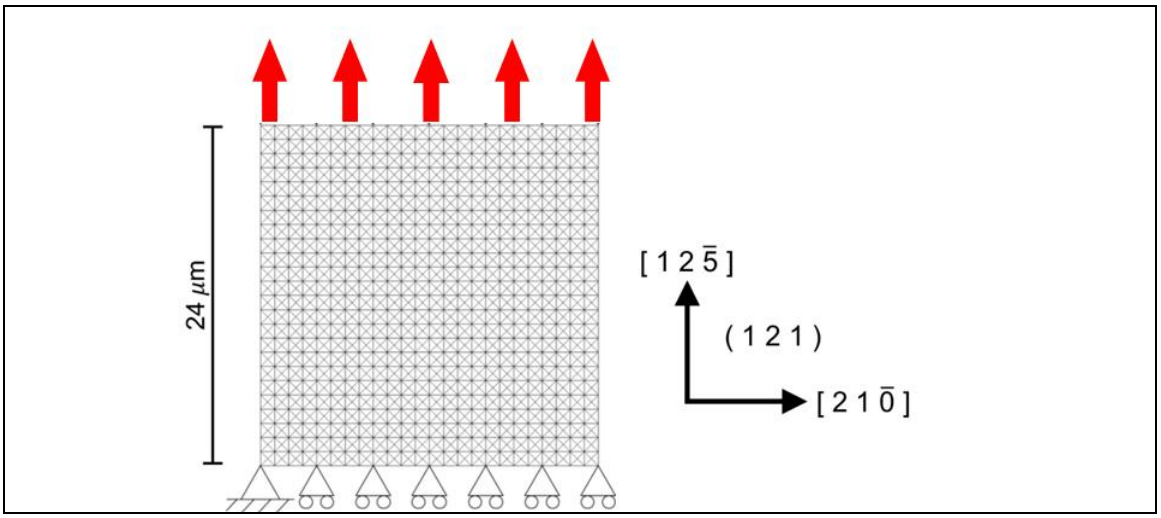

Figure 1. FE model used in tensile analysis, with loading axis promoting single slip.

Figure 2 displays representative results exhibiting nucleation and the following growth of twins under tension, together with the stress response accompanied by serration. The twinned regions yield lattice rotations that tend to saturate at around 20°. Contours denote twinned regions by frequency of meeting a critical resolved shear stress condition.

The twinning model becomes operative when the critical condition for the resolved shear stress is met, i.e., $\tau^{\chi} \geq \tau_{cr}^{t}$. Since nucleation and growth of twinned regions are generally difficult to predict using conventional constitutive models, other frameworks, such as phase field schemes, have been used elsewhere (*14*). The present FTMP-based model can also successfully simulate twinning as demonstrated here.

In the present simulations, nucleation sites of twinning are essentially controlled by precursor inhomogeneity due to slip. More precisely, the precursor inhomogeneity is evolved from the FTMP $\boldsymbol{\alpha}$ and $\boldsymbol{\eta}$ terms for the slip mode, i.e., $F_1(\alpha^{\beta}), F_2(\eta^{\beta})$ in equation 26, as shown in the top part of figure 2. This implies twinning behavior is greatly affected by the strain history.

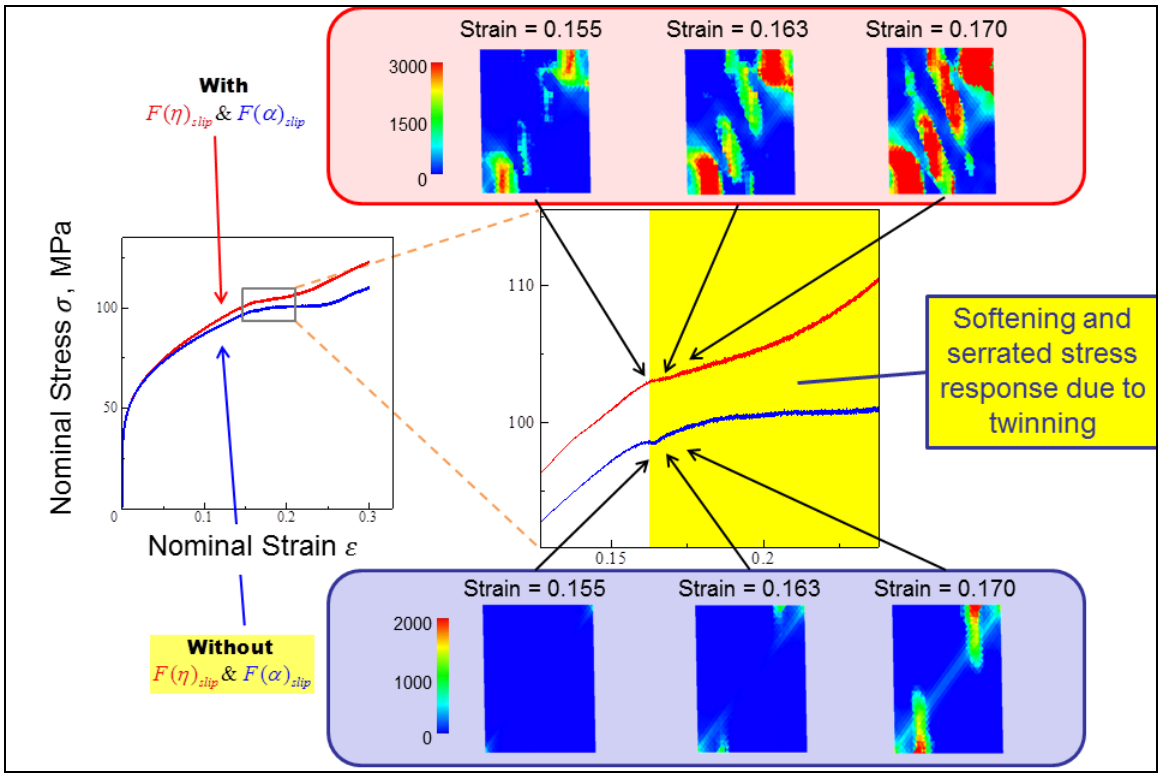

Figure 2. Stress-strain responses comparing effect of precursor inhomogeneity on twin evolution.

To demonstrate this implication, simulations are repeated with $F_1(\alpha^\beta), F_2(\eta^\beta) \to 0$, with results shown in the bottom part of figure 2. Nucleation of the twin in this case is delayed until $\varepsilon = 0.163$, and growth is ultimately initiated at around $\varepsilon = 0.170$, not from the center of the sample but from its upper and lower edges.

Figure 3 compares evolving contours of twinned regions as well as the incompatibility term $F(\eta)_{twin} \equiv F_3(\eta^\chi)$ between simulations considering the two conditions. Figure 3 confirms that weak evolution of slip-induced inhomogeneity, manifested as retarded growth of $F(\eta)_{twin}$, tends to inhibit the twin nucleation within the sample.

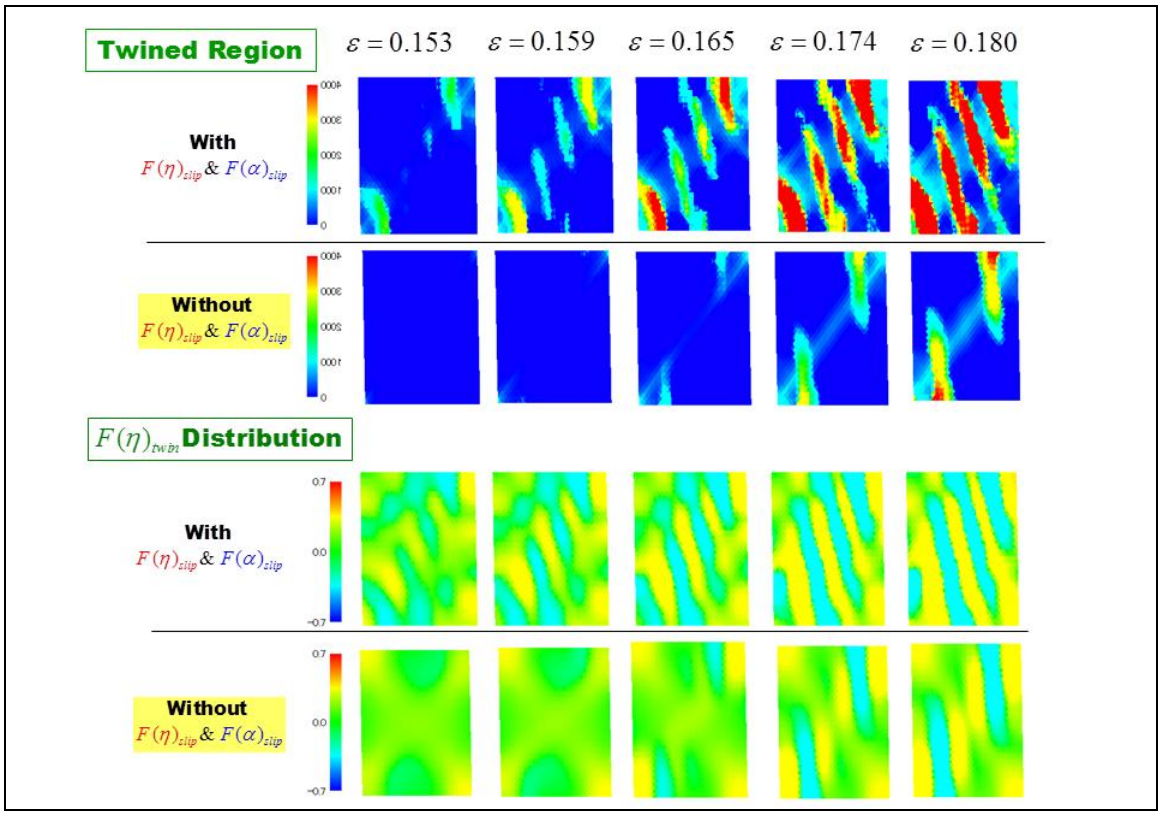

Figure 3. Comparison of twin domains (top) and incompatibility (bottom) for simulations with and without dislocation- and incompatibility-induced hardening.

5.2 Flow-Evolutionary Hypothesis and Duality Diagram

A duality diagram presentation permits observation of the associated energy flow from elastically stored states into local plasticity (dissipation) manifested by incompatibility tensor field evolutions. Specifically, such a diagram is constructed by plotting the trace of the incompatibility tensor $\mathrm{tr}\boldsymbol{\eta} = \eta_{KK}$ versus the fluctuating part of the elastic strain energy $\delta\mathcal{U}^e \approx \delta\mathcal{W}$ for a targeted domain, in further investigation of the hypothesis in equation 17.

To focus on twin nucleation phenomena, we selected an observation area in the central region of the domain, such that the intruding twinning from the upper lower edges is excluded, as indicated in figure 4.

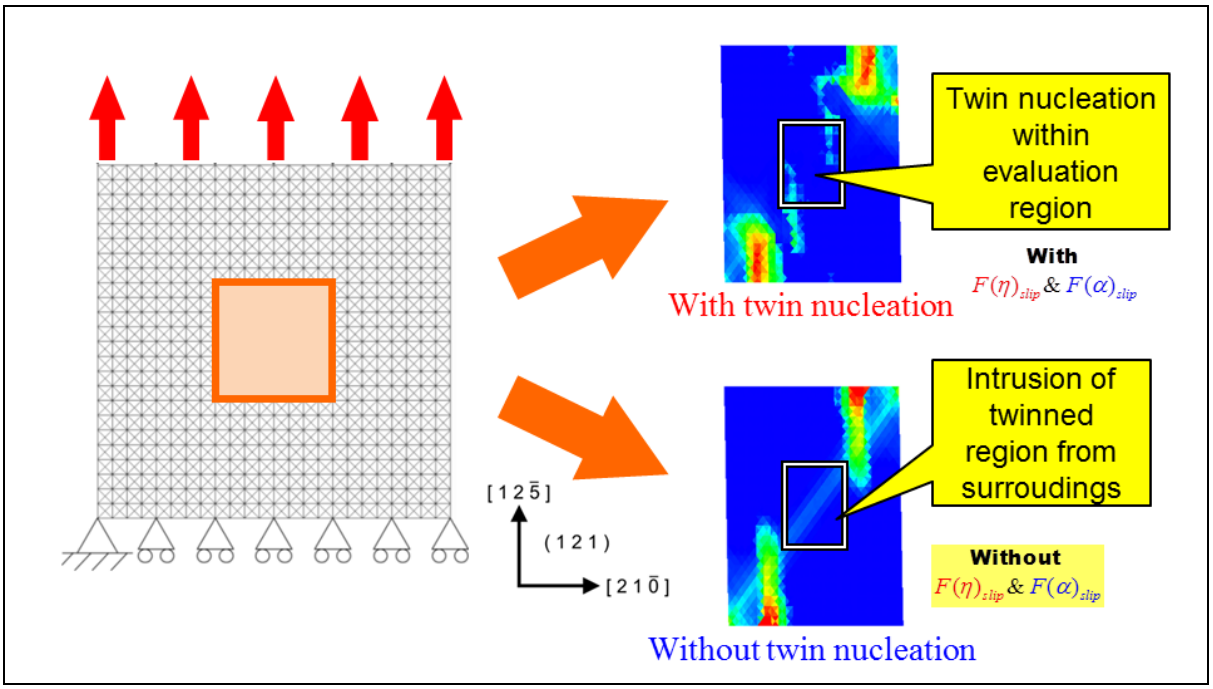

Figure 4. Observation area for duality diagram representations based on flow-evolutionary hypothesis comparing cases with and without twin nucleation.

Figure 5 shows duality diagrams for the observation area comparing the two model cases: those with and without twin nucleation. In figure 5, a sharp rise in the incompatibility η_{KK} is observed as strain energy $\mathcal{U}^e$ increases for both cases, but the case with twin nucleation shows much earlier onset of rise in η_{KK} than that without twin nucleation. Examining this more in detail, we see that the portion of the duality diagram where the sharp rises occur is enlarged in the inset. Marked differences between the two cases are clearly confirmed. The case with twin nucleation exhibits relatively gradual increase in η_{KK} with increasing strain energy $\mathcal{U}^e$ before nucleation takes place (marked by a circle). This pregrowth of η_{KK} corresponds to the evolution of the precursor inhomogeneity discussed already. The case without twin nucleation, in contrast, yields a much smaller growth rate of η_{KK}, eventually followed by a sharp increase not by nucleation but by intrusion of a twinned region from outside the observation area.

From the energetic point of view, the duality diagram provides the following insight. In the case with twin nucleation, a rapid release of energy that has been stored elastically into the twin degrees of freedom results in twin nucleation and subsequent growth.

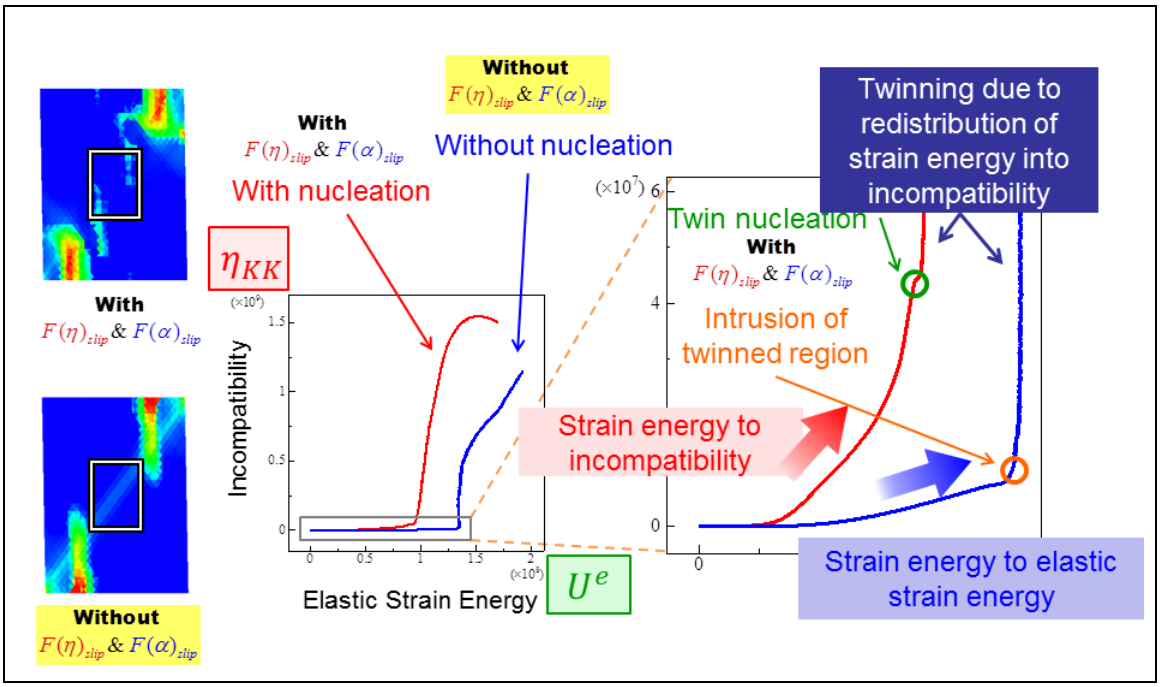

Figure 5. Duality diagram for FCC copper simulation results comparing cases with and without twin nucleation (with and without dislocation- and incompatibility-based hardening).

5.3 Summary

The foregoing results demonstrate some prominent capabilities of the proposed twinning model:

- Natural representations of twin nucleation are possible in the sense that no artificial disturbance that promotes the outset of the twinning is required.
- Nucleation and subsequent growth into lenticular shapes is realistically captured.
- Stress-strain responses accompanied by serration and overall softening are predicted.

The flow-evolutionary examination based on the duality diagram representation of the simulated results (tr$\boldsymbol{\eta}$ vs. $\delta\mathcal{U}^e$) has been shown indicative of twin evolution in terms of associated energy flow—specifically, how elastically stored strain energy is released to localized plastic flow or twinning. This has been clarified by comparing simulation results with and without the FTMP-η model, the latter in which such twinning evolution does not occur naturally.

6. Numerical Simulations: HCP Magnesium (Mg)

6.1 Model, Results, and Discussion

Based on the kinematic description for inelasticity of HCP metals—three families of slip systems (basal, pyramidal, and prismatic) and two twin systems (tensile and compression twins)—the FTMP-based model is now applied to Mg. Basic capabilities for modeling pure Mg, with mechanical properties and test data available in the literature, are also confirmed in this stage, e.g., anisotropy in single crystals, focusing on orientation-dependent stress-strain responses, contributions of the prismatic slip system, tension-compression asymmetric stress-strain responses, and strain rate effects including rate sensitivity of flow.

Deformation analyses are conducted for pure single-crystal Mg with the hexagonal crystal structure (termed here as hexagonal close packed or "HCP" following convention even though Mg does not demonstrate perfect close packing [*14*]), and descriptive capabilities of the model are confirmed by critical comparisons with experimental data for plane strain compression in multiple orientations from Kelley and Hosford (*15*, *16*).

Kelley and Hosford (*15*, *16*) conducted a systematic series of constrained compression experiments on Mg single crystals, as schematically illustrated in figure 6. In the present simulations, the die constraint condition is realistically mimicked by the plane strain assumption. Orientations E and F exhibit peculiar stress responses showing plateau-like stagnation followed by a rapid stress increase. The plateau-like stress response observed for these two orientations is thought to be an indication of twin activity as the dominant deformation mode, while rapid stress increase is only partially relieved by the onset of hard nonbasal slip modes when twinning has saturated. Orientation G is particularly soft because of its favorable Schmid factor for basal slip, which has much lower strength than other systems.

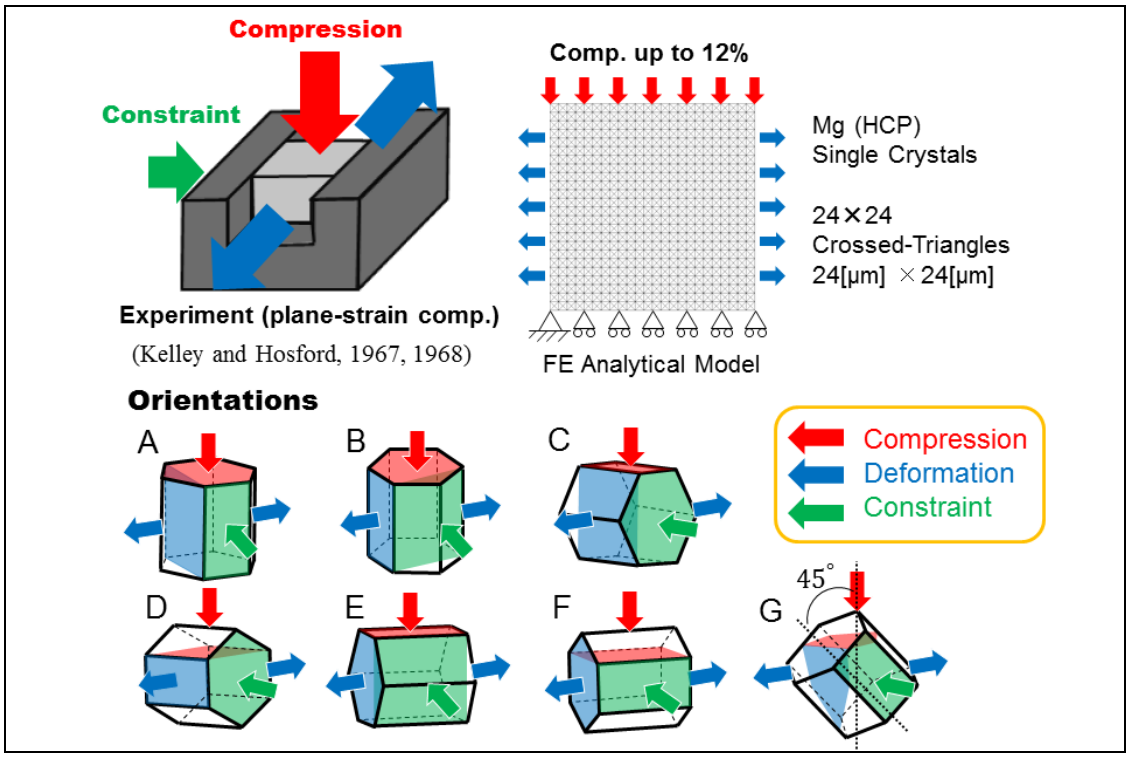

Figure 6. Simulations for plane strain compression of Mg single crystals; twinning is reported prevalent in experiments on crystals in orientations E and F (*15*, *16*).

Figure 7 shows the predicted stress-strain responses for orientations A–G (curves) compared with the experimental data (points). We obtained excellent agreement for all orientations. In particular, simulated results for orientations E and F successfully reproduce the rather unusual and highly nonlinear stress-strain responses induced by twinning.

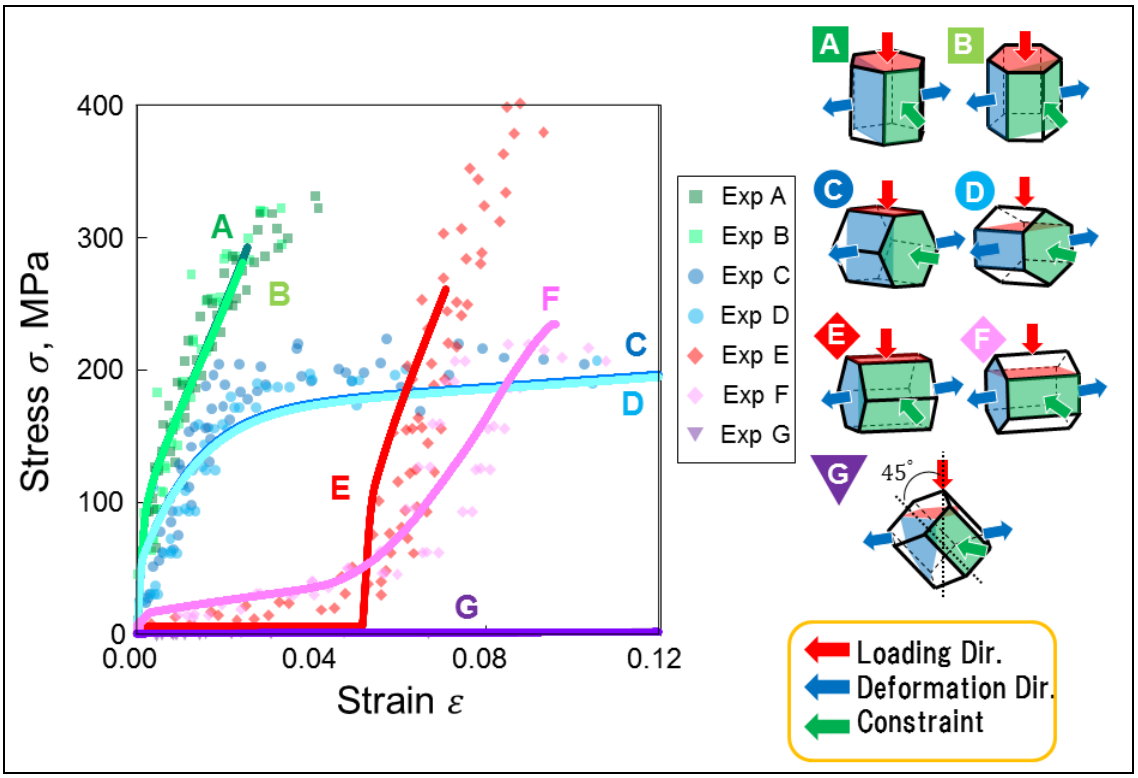

Figure 7. Compressive stress-strain predictions (curves) compared to experimental data for Mg (*15*, *16*).

6.2 Sample Size Dependence

One noteworthy feature of the present model is its ability to represent absolute scale conveyed through the evaluation range of the second spatial derivative of strain for obtaining the incompatibility tensor field in equation 10. Since the E and F orientations exhibit peculiar twin-dominated stress-strain responses, they are expected to be sensitively affected by sample dimensions. To explore this possibility, three domains are compared: 12×12, 24×24, and 48×48 μm^2. The associated results are presented in figure 8, together with stress-strain curves comparing the three sample sizes and the experimental data points. What can be clearly confirmed is that the emerging patterns obviously depend on the sample size for the two orientations. The stress responses vary slightly depending on the sample size, e.g., the onset of the stress rise for the E orientation is controlled by the sample dimension. The variation ranges roughly correspond to those of the experiments, implying the scatter of the experimental data may be a natural consequence of sample size or geometry.

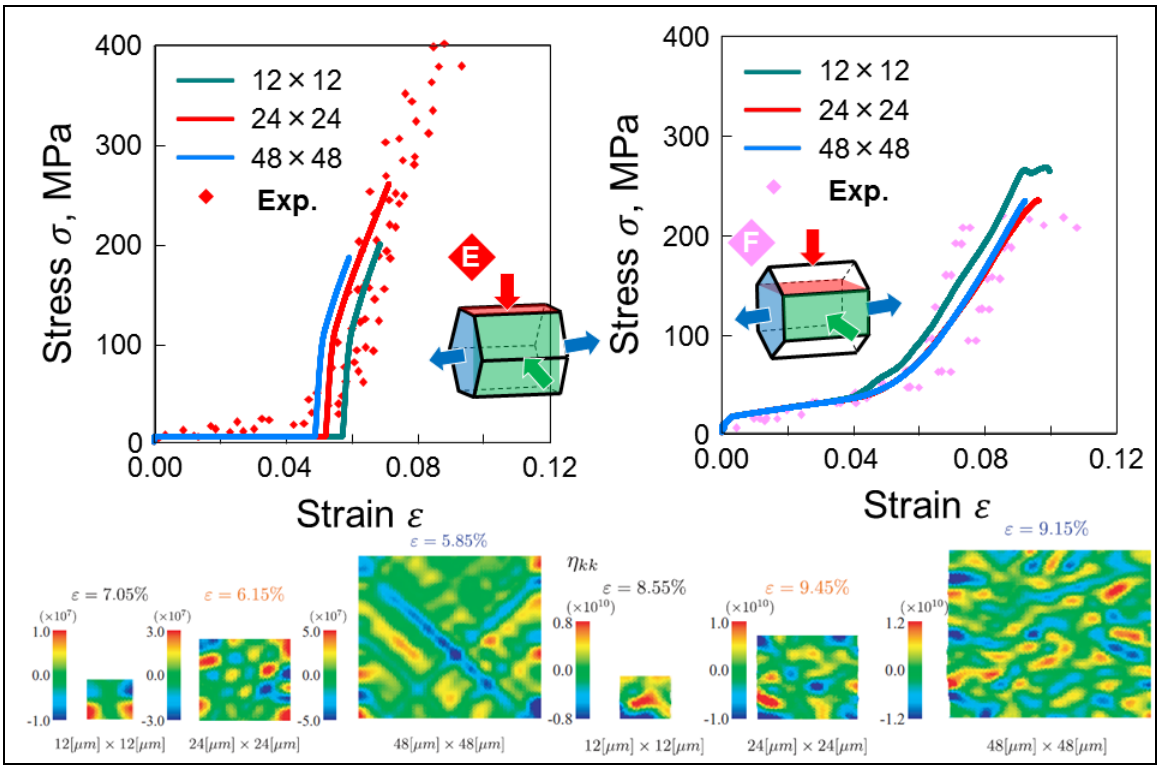

Figure 8. Stress-strain predictions and experimental data (top) and simulated strain contours (bottom) for differently sized simulation domains.

6.3 Mesh Size Independence

Another feature of the current modeling approach is its ability to produce mesh-independent results. To demonstrate this, we compared simulations with two mesh divisions, 24 × 24 and 48 × 48 crossed triangle elements with the same evaluation size for the incompatibility tensor calculation. Figure 9 shows strain contours for these domains with different mesh divisions. The same general patterns emerge regardless of mesh size. Corresponding stress-strain curves are also displayed, showing almost identical response.

For comparison, consider some recent conventional models for slip and twinning (*17*, *18*) that appear to introduce a mode transition condition between twinning and plastic slip in an ad hoc manner. For example, one such model (*17*) assumes a hardening law as

$$h(\gamma) = h_0 \text{ for } \gamma \le \gamma_{ref}, \quad h(\gamma) = h_0 (\gamma/\gamma_{ref})^{m-1} \text{ for } \gamma \ge \gamma_{ref}. \tag{33}$$

Because such models do not include scale effects or gradient/nonlocal terms, these tend to behave similarly regardless of sample geometry and size, which can be physically unrealistic.

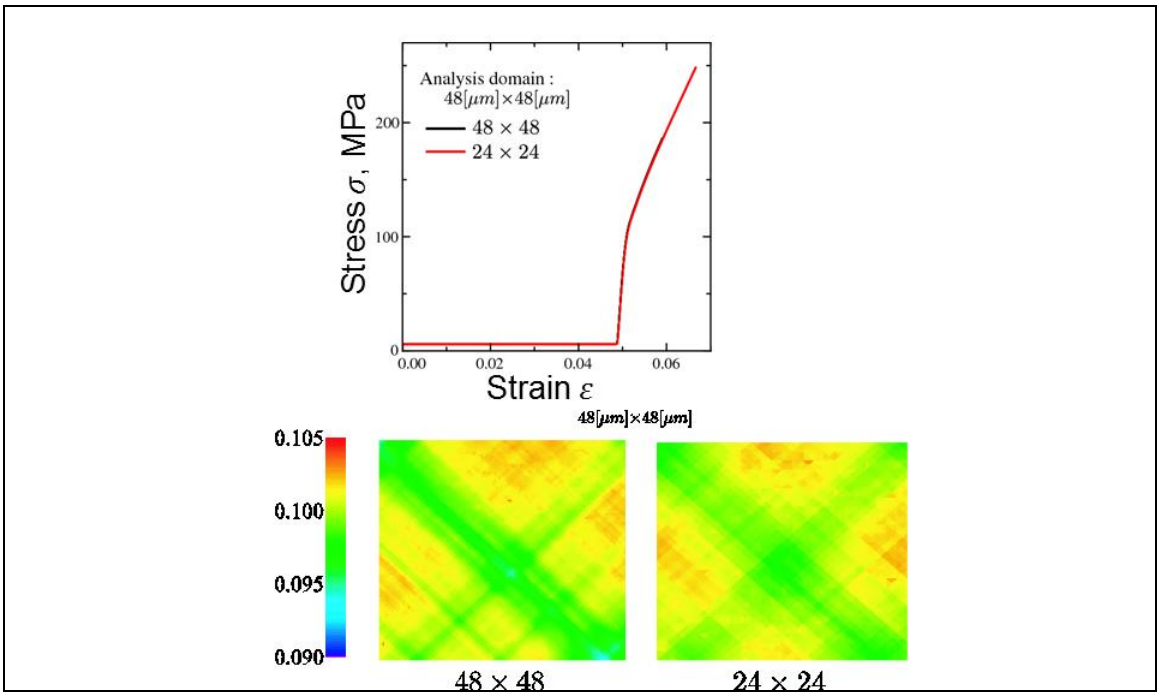

Figure 9. Stress-strain predictions (top) and strain contours (bottom) for domains with different meshes.

Phase field models, on the other hand, seem to enable consideration of size/scale effects since spatial gradients (e.g., of order parameter(s)) enter the constitutive response. However, we may need to introduce initial fluctuations in the phase field (twinned region, in this case), and, depending on the problem, this step may affect nucleation sites and the number of predicted equilibrium twinned regions. Therefore, this approach requires a sound rationale.

7. Conclusions

A new rational model for deformation twinning has been developed, extending the original FTMP theory of Hasebe for dislocation-based crystal plasticity. Twinning degrees of freedom are taken into account via the FTMP-based incompatibility model, which is further implemented into a crystalline plasticity constitutive framework via the hardening law. The FTMP-based model is applied first to study to a single slip-oriented FCC crystal, and preliminary simulations have been conducted under static conditions to confirm the model's basic capabilities. Simulation results exhibit nucleation and growth of twinned regions, accompanied by serrated stress responses with softening. The predicted nucleation of twins is examined in detail using duality diagrams in the context of Hasebe's flow-evolutionary hypothesis. Numerical simulations have also been performed for pure single-crystal magnesium with HCP structure, and descriptive

capabilities of the model have been confirmed by critical comparisons with experimental data for plane-strain compression of crystals of multiple orientations available in the literature. Results successfully reproduce the unique stress-strain responses induced by twinning. Activities of the various slip systems and twinning mechanisms for each orientation have been predicted. Other noteworthy features addressed here, but not captured by conventional continuum plasticity models, are sample size dependence and mesh size independence.

Future work will consider dynamic conditions with implementation using explicit FEM. Hypervelocity impact compression of metals will be explored, focusing on substructure evolution, where experimental observations have been documented in the literature.

8. References

1. Hasebe, T. Multiscale Crystal Plasticity Modeling Based on Field Theory. *Comp. Mech. Eng. Sci.* (*CMES*), **2006**, *11*, 145–155.
2. Hasebe, T. Continuum Description of Inhomogeneously Deforming Polycrystalline Aggregate Based on Field Theory. In *Meso-Scale Simulation and Modeling of Strength and Fracture of Materials, IUTAM Symposium on Mesoscopic Dynamics of Fracture Process and Materials Strength*; Kitagawa, H., Shibutani, Y., Eds.; Kluwer: Dordrecht, The Netherlands, 2004; pp 381–390.
3. Hasebe, T. Field Theoretical Multiscale Modeling of Polycrystal Plasticity. *Trans. MRS-J* **2004**, *29*, 3619–3624.
4. Hasebe, T. *Field Theory of Multiscale Plasticity*; Cambridge University Press: Cambridge, UK, 2013.
5. Clayton, J. D. On Anholonomic Deformation, Geometry, and Differentiation. *Mathematics and Mechanics of Solids* **2012**, *17*, 702–735.
6. Clayton, J. D. *Nonlinear Mechanics of Crystals*; Springer: Dordrecht, The Netherlands, 2011.
7. Marcinkowski, M. J. *Unified Theory of the Mechanical Behavior of Matter*; Wiley: New York, 1979.
8. Aoyagi, Y.; Hasebe, T. New Physical Interpretation of Incompatibility Tensor and Its Application to Dislocation Substructure Evolution. *Key Engineering Materials* **2007**, *340–341*, 217–222.
9. Maugin, G. A. *Material Inhomogeneities in Elasticity*; Chapman & Hall: London, 1993.
10. McDavid, A. W.; McMullen, C. D. Generalizing Cross Products and Maxwell's Equations to Universal Extra Dimension. http://arxiv.org/abs/hep-ph/ (accessed 2006).
11. Hasebe, T. Interaction Fields Based on Incompatibility Tensor in Field Theory of Plasticity—Part I: Theory. *Interaction and Multiscale Mechanics* **2009**, *2*, 1–14.
12. Hasebe, T. Interaction Fields Based on Incompatibility Tensor in Field Theory of Plasticity—Part II: Application. *Interaction and Multiscale Mechanics* **2009**, *2*, 15–30.
13. Clayton, J. D. A Continuum Description of Nonlinear Elasticity, Slip and Twinning, With Application to Sapphire. *Proc. R. Soc. Lond. A* **2009**, *465*, 307–334.

14. Clayton, J. D.; Knap, J. A. Phase Field Model of Deformation Twinning: Nonlinear Theory and Numerical Simulations. *Physica D* **2011**, *240*, 841–858.

15. Kelly, E. W.; Hosford, W. F. Plane-Strain Compression of Magnesium and Magnesium Alloy Crystals. *Trans. Metall. Soc. AIME* **1967**, *242*, 5–13.

16. Kelly, E. W.; Hosford, W. F. The Deformation Characteristics of Textured Magnesium. *Trans. Metall. Soc. AIME* **1968**, *242*, 654–661.

17. Graff, S.; Steglich, D.; Brocks, W. Forming of Magnesium-Crystal Plasticity and Plastic Potentials. *Adv. Eng. Mater*. **2007**, *9*, 803–806.

18. Zhang, J.; Josh, S. P. Phenomenological Crystal Plasticity Modeling and Detailed Micromechanical Investigations of Pure Magnesium. *J. Mech. Phys. Solids* **2012**, *60*, 945–972.

NO. OF COPIES	ORGANIZATION
1 (PDF)	DEFENSE TECHNICAL INFORMATION CTR DTIC OCA
1 (PDF)	DIRECTOR US ARMY RESEARCH LAB IMAL HRA
1 (PDF)	DIRECTOR US ARMY RESEARCH LAB RDRL CIO LL
1 (PDF)	GOVT PRINTG OFC A MALHOTRA
1 (PDF)	RDRL WMP C J CLAYTON

INTENTIONALLY LEFT BLANK.